Negligible magnetic losses at low temperatures in liquid phase epitaxy grown $Y_3Fe_5O_{12}$ films

A. R. Will-Cole,[1,2] James L. Hart,[3] Valeria Lauter,[4] Alexander Grutter,[5] Carsten Dubs,[6] Morris Lindner,[6] Timmy Reimann,[6] Nichole R. Valdez,[2] Charles J. Pearce,[2] Todd C. Monson,[2] Judy J. Cha,[3] Don Heiman,[7,8] and Nian X. Sun[1]

[1]*Electrical and Computer Engineering Department, Northeastern University, Boston, Massachusetts 02115, USA*
[2]*Sandia National Laboratories, Albuquerque, New Mexico 87123, USA*
[3]*Materials Science and Engineering Department, Cornell University, Ithaca, New York 14853, USA*
[4]*Spallation Neutron Source, Oak Ridge National Laboratory, Oak Ridge, Tennessee 37830, USA*
[5]*Center for High Resolution Neutron Scattering, National Institute of Standards and Technology, Gaithersburg, Maryland 37830, USA*
[6]*INNOVENT e.V. Technologieentwicklung, Prüssingstrasse 27B, 07745 Jena, Germany*
[7]*Physics Department, Northeastern University, Boston, Massachusetts 02115, USA*
[8]*Plasma Science and Fusion Center, Massachusetts Institute of Technology, Cambridge, Massachusetts 02139, USA*

(Received 3 March 2023; accepted 12 May 2023; published 31 May 2023)

Yttrium iron garnet ($Y_3Fe_5O_{12}$; YIG) has a unique combination of low magnetic damping, high spin-wave conductivity, and insulating properties that make it a highly attractive material for a variety of applications in the fields of magnetics and spintronics. While the room-temperature magnetization dynamics of YIG have been extensively studied, there are limited reports correlating the low-temperature magnetization dynamics to the material structure or growth method. Here we investigate liquid phase epitaxy grown YIG films and their magnetization dynamics at temperatures down to 10 K. We show there is a negligible increase in the ferromagnetic resonance linewidth down to 10 K, which is unique when compared with YIG films grown by other deposition methods. From the broadband ferromagnetic resonance measurements, polarized neutron reflectivity, and scanning transmission electron microscopy, we conclude that these liquid phase epitaxy grown films have negligible rare-earth impurities present, specifically the suppression of Gd diffusion from the $Gd_3Ga_5O_{12}$ (GGG) substrate into the $Y_3Fe_5O_{12}$ film, and therefore negligible magnetic losses attributed to the slow-relaxation mechanism. Overall, liquid phase epitaxy YIG films have a YIG/GGG interface that is five times sharper and have ten times lower ferromagnetic resonance linewidths below 50 K than comparable YIG films by other deposition methods. Thus, liquid phase epitaxy grown YIG films are ideal for low-temperature experiments/applications that require low magnetic losses, such as quantum transduction and manipulation via magnon coupling.

DOI: 10.1103/PhysRevMaterials.7.054411

I. INTRODUCTION

Yttrium iron garnet ($Y_3Fe_5O_{12}$, also known as YIG) has received a lot of attention in the magnetics and spintronics communities due to its low magnetic damping parameter and high magnon/spin-wave conductivity at room temperature [1–3]. The intrinsic magnetic damping parameter is as low as $\alpha \simeq 3 \times 10^{-5}$ [4,5], while the lowest reported magnetic damping parameter to date for thin films is $\alpha \approx 5.2 \times 10^{-5}$ [6]. The low magnetic damping in YIG enables long spin-wave decay lengths in excess of 100 μm [7,8]. In addition to the low magnetic damping parameter and high magnon/spin-wave conductivity, YIG is of interest with respect to its spin-current related behavior. Namely, magnetization excitations in YIG films can inject a pure spin current into adjacent nonmagnetic metal through spin pumping or the spin Seebeck effect [3,9]. Additionally, injected charge current in a nonmagnetic metal can be converted to spin current through spin-orbit coupling and subsequent applied spin torque on the adjacent YIG [10]. Therefore, there is extensive research focused on the magnetization dynamics in YIG/Pt bilayer structures via spin pumping, spin torque, and laser-driven excitations [11–16].

Thin-film YIG has been grown with a variety of deposition methods including pulsed laser deposition [17–19], magnetron sputtering [6,20], molecular beam epitaxy [21,22], and liquid phase epitaxy (LPE) [23,24]. Scalability is essential for commercial integration of YIG, therefore magnetron sputtering and LPE [25] are two viable deposition approaches of particular importance. A key challenge for commercial YIG integration is the lattice-matching requirement for epitaxy. Most YIG films must be grown on $Gd_3Ga_5O_{12}$ (GGG) since GGG has the same garnet structure as YIG with a lattice constant of 12.383 Å [26–28]. Additionally, in the (111) orientation there is only a 0.06% in-plane lattice mismatch between YIG and GGG. While the GGG substrate allows for heteroepitaxial growth of YIG films, the GGG substrate can serve as a source of contamination in the YIG films. Polarized neutron reflectivity studies on YIG/GGG revealed there is selective Gd diffusion from the GGG substrate into the YIG film which locally suppresses the magnetization, leading to an ∼ 5-nm magnetic dead layer [29–31]. Magnetic dead layers in YIG films can also form from selective Ga diffusion into the YIG film [32]. Another source of contamination in YIG films is from the pulsed laser deposition or sputtering target material impurities. For example, a Y_2O_3 target with

99.99% purity can contain Dy atoms at a concentration of 5×10^{-5} [33]. Rare-earth impurities are known to serve as an additional loss mechanism in YIG films at low temperatures, known as the slow-relaxation phenomenon [5,34,35]. The relaxation depends on the exchange coupling between spins of the Fe sites and the impurity elements present as well as the coupling of the impurity spins to the lattice [34]. While magnetization dynamics of thin-film YIG have been extensively studied at room temperature, there are limited temperature-dependent studies. Many studies on YIG films, both undoped and intentionally doped with rare-earth elements, report signatures of slow relaxation due to the presence of rare-earth dopants and/or impurities [20,32,34,36,37].

The low-temperature performance of magnetic insulators is critical for applications related to quantum transduction. The coherent interaction between phonons, photons, spin-wave modes, and qubits can enable complex hybrid systems [38,39]. Such proposed quantum transduction platforms require low temperatures to mitigate acoustic losses, and to reduce thermal noise that may lead qubits to decohere. An advantage of utilizing YIG in such a hybrid quantum system is that the low magnetic losses can enhance the cooperativity and strength of coupling for these hybridized modes [38]. However, if the YIG suffers significantly from the slow-relaxation phenomenon at the operation temperatures of interest, this can greatly increase the loss rate of the system due to the increased magnetic losses. Thus, the YIG films need to have minimal contributions to magnetic loss due to rare-earth impurities. Here we report LPE grown YIG films with minimal rare-earth impurity contributions compared with other state-of-the-art YIG thin films. We show there is a negligible increase in ferromagnetic resonance linewidth down to 10 K, which to our knowledge, is the only YIG film reported in literature with such low magnetic loss at these low temperatures. We substantiate our film quality with additional characterization, i.e., x-ray diffraction (XRD), polarized neutron reflectivity (PNR), and scanning transmission electron microscopy (STEM), which indicate there is suppressed Gd diffusion across the YIG/GGG interface unlike other comparable films.

II. RESULTS AND DISCUSSION

The YIG films were grown by LPE at INNOVENT in Jena, Germany, on GGG(111) substrates from a PbO-B_2O_3–based high temperature at about 800 °C via the standard isothermal dipping technique [23,40]. The purity of the Y_2O_3 source material was 99.999% (referenced with respect to the total amount of rare-earth oxides). The epiready GGG substrates purchased from Luxium Solutions in clean room packing were placed in the substrate holder prior to growth and immediately transferred into the furnace to keep them free of contamination. For further details on the liquid phase epitaxy deposition of YIG on GGG(111) we refer to Ref. [23]. The x-ray reflectivity (XRR) characterization was performed on a Rigaku SmartLab diffractometer with a Cu $K\alpha$ source and the XRD characterization was performed on a Bruker D8 Discover diffractometer with a Cu $K\alpha$ source [41]. The thicknesses of the films explored here were determined to be approximately 48 nm (used for magnetic measurements) and 50 nm (used for PNR and STEM) via XRR measurements with an average root-mean-square roughness of ∼0.32 nm. The representative raw data and model for the XRR measurement is provided in Fig. 1(a). The XRD pattern is provided in Fig. 1(b). We observe in these (111)-oriented films pronounced Laue oscillations at the (444) and the (888) Bragg reflections. The Laue oscillations are caused by the phase difference between the x rays reflected from the sample surface and those reflected at the interface with the substrate. They only occur in the case of highly uniform, single-crystalline ordered films with smooth interfaces. The overlap of the (444) and (888) reflections seems to be perfect, as the YIG and GGG peaks cannot be separated from each other. Therefore, these results indicate that the YIG film grew perfect lattice matched on the GGG substrate. From the (444)-peak and the (888)-peak positions we find that the average out-of-plane spacing between adjacent YIG(111) planes is 7.135 Å, and assuming the cubic garnet structure, that the a-lattice constant is 12.358 Å, which is quite close to the YIG bulk a-lattice constant of 12.376 Å.

To further characterize the structural and magnetic quality of the LPE grown YIG/GGG, we performed PNR using the magnetism reflectometer at the Spallation Neutron Source at Oak Ridge National Laboratory [42,43]. PNR is sensitive to the depth profiles of the nuclear (ρ_N) and magnetic (ρ_M) scattering length densities (SLDs) of the heterostructure. The nuclear SLD is determined by the density and composition of the scattering material, while the magnetic SLD is determined by the net in-plane magnetization. Simultaneous depth-resolved information (resolution of 0.5 nm) about the heterostructure composition, density, and magnetization can therefore be obtained by fitting the PNR data, making it an ideal technique for obtaining information about the YIG film and the YIG/GGG interface. Measurements were conducted in a closed cycle refrigerator equipped with an electromagnet. For these measurements, the samples were saturated in a field of 0.5 T, far exceeding the saturation field of the sample of <0.5 mT. For the PNR measurement, a spin-polarized neutron beam was incident on the sample, while a spin flipper was used to select the incoming neutron spin state so that measurements could be performed with both spin-up and spin-down neutrons. The spin-dependent neutron reflectivity spectra, $R+$ (neutron spin parallel) and $R-$ (neutron spin antiparallel to the direction of the external magnetic field), were measured as a function of the wave vector transfer vector, $Q = 4\pi \sin(\theta)/\lambda$, along the direction normal to the film surface. The measurements were collected at 300 K first, and then the sample was field cooled at 0.5 T down to 100 K where the second measurement was performed. The sample size was 8 mm × 8 mm for the PNR measurements in an effort to reduce the neutron count time required for the high-Q measurements. The reflectivity data was fit using the REFL1D software package as shown in Fig. 2. From the model fit we obtained the nuclear and magnetic SLDs as a function of the distance from the substrate. Initially, our model consisted of a GGG substrate, an additional layer at the interface, and the YIG film, which is the model obtained by other PNR studies on YIG/GGG by Mitra *et al.* and Cooper *et al.* [29,30]. However, comparison with a simpler two-layer model, consisting of just the GGG substrate and the YIG film, revealed that the additional interfacial layer did not significantly improve

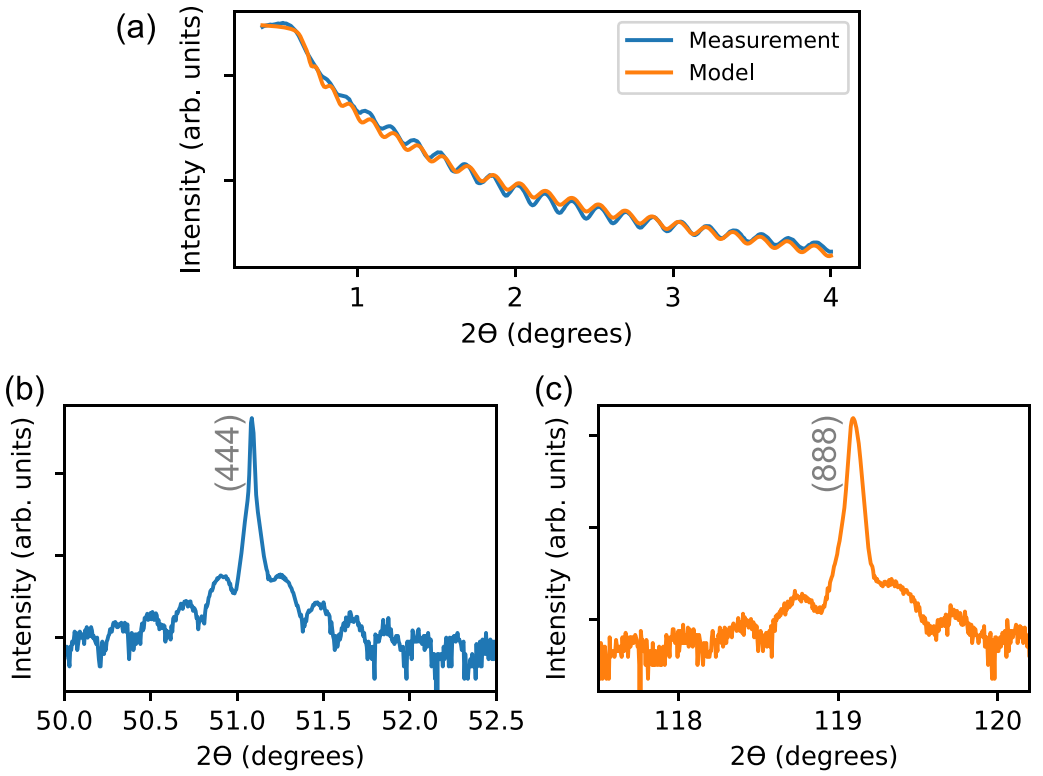

FIG. 1. (a) X-ray reflectivity data and model fit for YIG/GGG. (b) X-ray diffraction spectra of YIG/GGG at the (444) Bragg reflection. (c) X-ray diffraction spectra of YIG/GGG at the (888) Bragg reflection. Both (b) and (c) show pronounced Laue oscillations and the reflections of the film and substrate are perfectly superimposed with no resolvable lattice misfit.

the fit for these samples. This is in stark contrast to previous reports in the literature on sputtered YIG films, which strictly require the inclusion of a chemically and magnetically distinct interfacial layer to achieve a good fit [29,30]. The distinction between our model and that of the models in literature obtained for sputtered YIG/GGG is that our nuclear and magnetic SLD profile exhibits a sharp transition across the YIG/GGG interface at both 100 and 300 K, as shown in Fig. 2(d). Previous results on sputtered YIG/GGG report a negative magnetic scattering length density across the YIG/GGG interface indicative of Gd diffusion and antiparallel Gd moment ordering with respect to the YIG moment below 150 K, and significant magnetically dead layers above this temperature [29]. From our PNR measurement we can conclude that the LPE grown YIG film on GGG has an abrupt interface without any significant Gd diffusion or magnetization suppression and therefore the LPE YIG/GGG interface is superior to sputtered films. Additionally, we can calculate the in-plane magnetization at saturation of the YIG film because the magnetic SLD, ρ_M, is related to the magnetization, M—the relation is given in Eqs. (1) and (2).

$$\rho_M = \mp \frac{m}{2\pi\hbar^2}\mu B\,, \tag{1}$$

$$M = \rho_M/(2.853 \times 10^{-9}\ \text{Å}^{-2}\ \text{m/kA}). \tag{2}$$

In Eq. (1) m is the moment, $\hbar$ is Planck's constant, μ is the neutron magnetic moment $(-1.913 \times 5.051 \times 10^{-27}\ \text{J/T})$, and B is the magnetic field. Note that 1 $\text{cm}^3/\text{emu} = 1$ m/kA. Based on Eq. (2) the magnetization at 300 K is determined to be 1757 G (1 kA/m $= 4\pi$ G), which is consistent with the usually reported saturation magnetization of YIG/GGG films at 1750 G [1]. At 100 K the YIG magnetization increases to 2458 G. The advantage of using PNR to extract the true magnetization value is that it is for the YIG film alone and is not convoluted with the moment arising from the strongly paramagnetic GGG substrate.

We performed high angle annular dark-field scanning transmission electron microscopy (HAADF-STEM) to confirm the interfacial sharpness of the YIG/GGG interface that was inferred through the PNR measurement and modeling. The cross-sectional STEM specimen was prepared with the standard focused ion beam (FIB) lift-out method, using a Thermo Fisher Scientific (TFS) Helios G4 X FIB, with final thinning performed at 2 kV. HAADF-STEM and electron energy loss spectroscopy (EELS) measurements were obtained using an aberration-corrected TFS Titan Themis 300 X-FEG, equipped with a Gatan GIF Tridiem energy filter. The microscope was operated at 300 kV, with a < 100 pA beam current, and a convergence semiangle of 30 mrad. The HAADF-STEM images of the interface observed along the [112]-type axis reveal a sharp transition of the intensity from the GGG substrate across to the YIG film as previously shown by Dubs *et al.* for an 11-nm thin LPE YIG layer [23]; a representative image is shown in Fig. 3(a) and this sharp interface is observed throughout the entire sample. Note for the HAADF image in Fig. 3(a), a stack of 20 images was collected, aligned, and summed. In the HAADF-STEM imaging mode the contrast scales with the atomic number, Z, of the material, where the most significant Z contrast is between the Y and Gd sites. Therefore, inspection of this image provides reliable qualita-

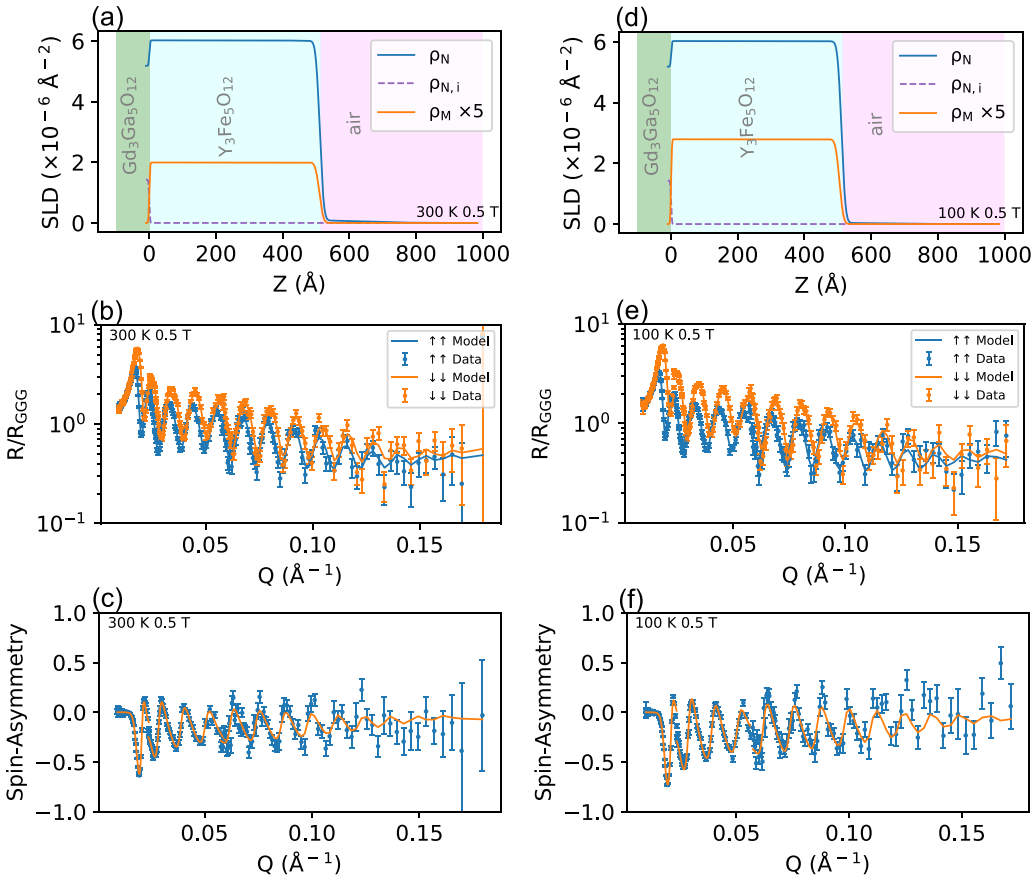

FIG. 2. Displayed are the model profile for the nuclear (ρ_N), imaginary part of the nuclear ($\rho_{N,i}$), and magnetic (ρ_M) scattering length density for measurements taken at (a) 300 and (d) 100 K, the Fresnel reflectivity plots for spin-up and spin-down neutrons along with their model fit for measurements taken at (b) 300 and (e) 100 K, and the spin asymmetry along with the model fit for measurements taken at (c) 300 and (f) 100 K. Error bars represent ± 1 standard deviation.

tive evidence that the YIG/GGG interface is sharp with limited Gd diffusion relative to reported observations in equivalent sputtered films (typical to have 5-10-nm-wide interdiffusion regions at the sputtered YIG/GGG interface) [29,30]. The EELS measurement provides further confirmation that the Gd remains tightly confined within the GGG substrate. The EELS data in Figs. 3(b) and 3(c) were taken from a two-dimensional spectrum image. The data was summed parallel to the interface over 14 nm to improve the signal-to-noise ratio. A power-law background subtraction was performed, as implemented in GATAN DIGITAL MICROGRAPH. For Fig. 3(b) the extracted EELS spectra show the Fe L edge, the Ga L edge, and the Gd M edge. As marked with the colored arrows in Fig. 3(a), the spectra are spaced 0.35 nm apart, therefore we can map the chemistry of each (222) plane across the interface. There are a few atomic planes that show the coexistence of Fe and Gd; however, the Gd signal decays rapidly within the YIG film. Shown in Fig. 3(c) are the EELS line profiles for Fe, Y, Gd, and Ga, as well as a HAADF line profile across the interface. For all the signals, the normalized signal intensity falls from 0.9 to 0.1 within a 1.2 nm distance, hence, the measured interface thickness is $\approx$1.2 nm. However, given the specimen chemistry and thickness, $\sim$0.5 nm of signal delocalization is expected [40]. Thus, the true interface thickness is likely <1 nm. This interface thickness is consistent with the previously obtained transition width of 1.9 nm $\pm$ 0.4 nm for 11-nm thin LPE YIG [22]. This value is considerably lower than those found in sputtered films, which show interfacial regions on the order of 5-10 nm. To estimate the Gd composition across the interface we analyze the intensity of the Gd M_5 peak after background subtraction. By assuming that the GGG substrate is stoichiometric (with a Gd concentration of 15 at. %), we convert the measured Gd peak intensities to Gd at. % for EELS measurements across the interface. For the spectra shown in Fig. 3(b), the estimated layer-resolved Gd compositions in atomic percent are (starting in the GGG substrate and moving into the YIG film) 15.1, 15.0, 14.9, 14.4, 11.6, 5.8, 2.2, 1.0, 0.6, $\leqslant$0.2, $\leqslant$0.2, with an estimated measurement uncertainty of 0.2 at. %. The exceptionally sharp interface with minimal Gd interdiffusion explains the absence of a magnetic dead layer, as determined from PNR. A zoomed-out image highlighting the uniformity of the YIG film and the YIG/GGG interface is provided in the Supplemental Material (Fig. S1). See the Supplemental Material for the additional STEM image [44].

To understand how the sharper interface influences the temperature-dependent magnetization dynamics, we measured the ferromagnetic resonance (FMR) response using a broadband coplanar waveguide with a flipped-chip configuration installed in a physical property measurement system

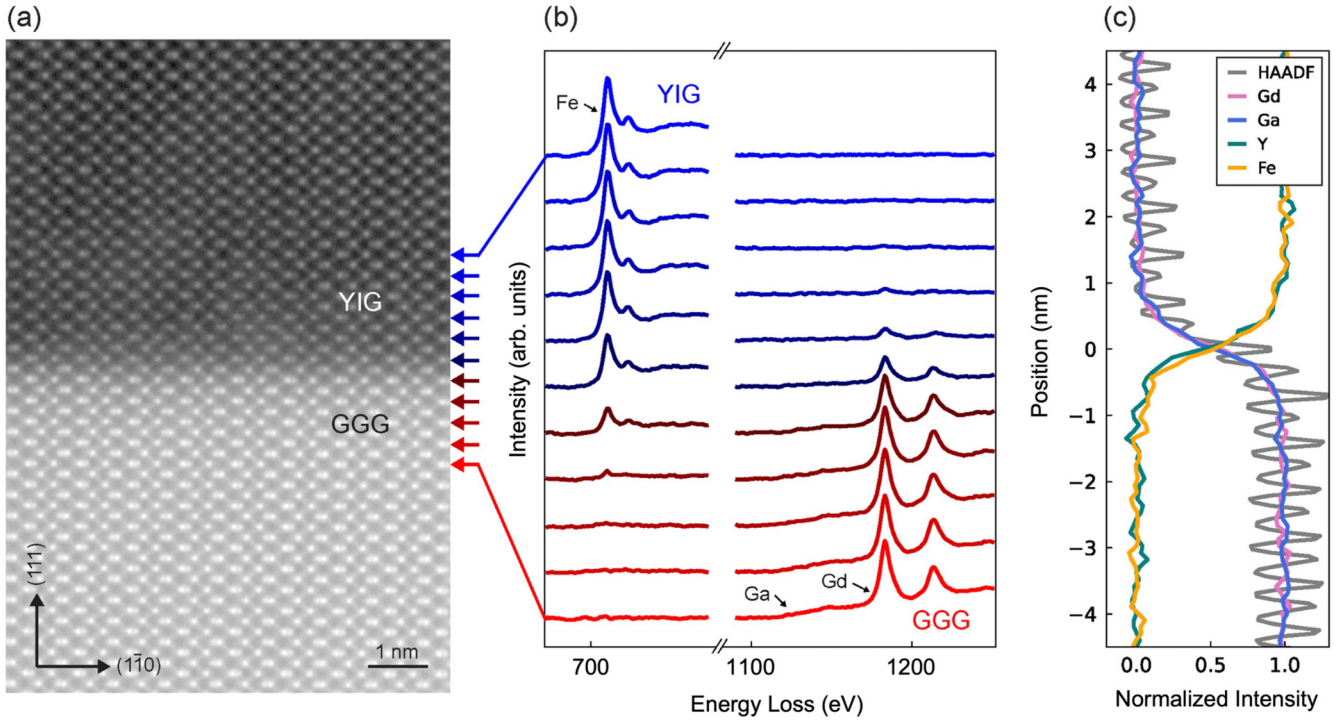

FIG. 3. (a) HAADF-STEM representative image of the YIG/GGG interface. (b) EELS spectra across the YIG/GGG interface. The arrows in (a) correspond to the atomic plane of each consecutive spectra in (b). (c) HAADF and EELS intensity profiles across the YIG/GGG interface. Note that the Y signal comes from the Y L edge at ∼2080 eV. The HAADF intensity is provided in the gray trace, the Gd in the pink trace, Ga in the blue trace, Y in the green trace, and Fe in the gold trace.

with a He cooling capability. Magnetic field sweep FMR measurements yielded a differential absorption spectrum at each frequency (f), and here we focused on the derivative peak corresponding to the main resonance uniform mode. The frequency used in the FMR measurement varied from 3 to 12 GHz, and the sample temperature ranged from 10 to 300 K. The FMR spectra and data fits (Gilbert damping and Kittel) are provided in the Supplemental Material (Figs. S2–S7) [44]. The effective in-plane magnetization and gyromagnetic ratio was extracted from the FMR data using the Kittel equation provided in Eq. (3), where H_{RES} is the resonance field, γ is the gyromagnetic ratio, and $4\pi M_{\mathrm{eff}}$ is the effective in-plane magnetization.

$$f = |\gamma/2\pi|\sqrt{H_{\mathrm{RES}}(H_{\mathrm{RES}} + 4\pi M_{\mathrm{eff}})}. \tag{3}$$

In Fig. 4(a) the extracted in-plane magnetization is plotted as a function of temperature for the YIG/GGG. Additionally, Fig. 4(a) includes the magnetization values extracted from the PNR data using Eq. (1). The data was fit on the basis of the traditional Bloch $T^{3/2}$ law, which describes the temperature dependence of the magnetization for materials with spontaneous magnetic ordering. We conclude that there is no significant magnetization suppression at the YIG/GGG interface since the magnetization versus temperature data follows the Bloch law dependence. We cannot comment on the Curie temperature, because we have only probed the effective magnetization from the FMR measurement, which includes the anisotropy field contribution not determined here since we can only access an in-plane orientation here [45,46]. In Fig. 4(b) the extracted gyromagnetic ratio is plotted as a function of temperature for the YIG/GGG. The gyromagnetic ratio is typically assumed to be 28 GHz/T for magnetic materials. Here we see a slight temperature dependence in the gyromagnetic ratio with an approximate 0.2 GHz/T decrease from room temperature to 10 K in contrast to the trend found in bulk YIG [47]. The Gilbert damping constant was extracted from a linear fit to $\Delta H/\Delta f$ as a function of frequency using the relation provided in Eq. (4), where $\Delta\eta_{FWHM}$ is the uniform mode linewidth, ΔH_0 is the inhomogeneous linewidth broadening, and γ is the gyromagnetic ratio (extracted from the Kittel equation) [48].

$$\Delta\eta_{\mathrm{FWHM}} = \Delta H_0 + \frac{2\pi\alpha}{\gamma}. \tag{4}$$

In Figs. 4(c) and 4(d) the extracted damping parameter and inhomogeneous linewidth broadening are shown, respectively. The damping parameter increases as a function of decreasing temperature with a peak damping parameter at ∼25 K. In contrast, Haidar *et al.* reported that the damping parameter decreases with decreasing temperatures for pulsed laser deposited YIG films [33]. However, the films in Haidar *et al.* have an order of magnitude higher damping compared to best-in-class LPE YIG films, and below 10 K the damping values are three times higher than LPE YIG films. Therefore, the behavior cannot be directly compared since subtle effects may be masked by the large damping reported in Haidar *et al.* [33].

To understand how the sharper interface influences the FMR linewidth versus temperature trend we collected a differential absorption spectrum at a set frequency (8 and 12 GHz)

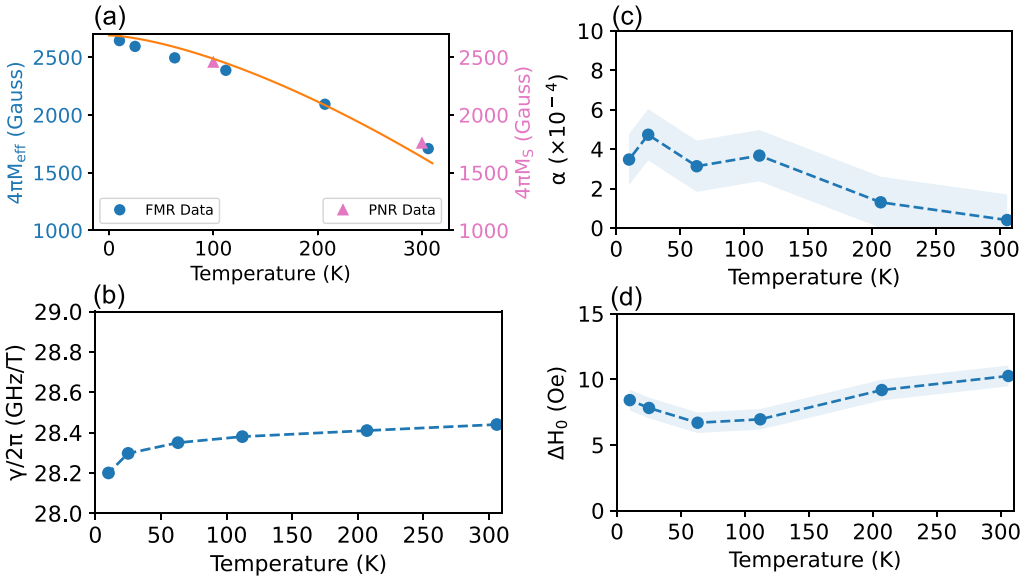

FIG. 4. (a) The extracted in-plane magnetization is plotted as a function of temperature for the YIG/GGG. The orange line is the fitting to the Bloch law of $M(T) = M(0)[1\text{-}(T/T_c)^{3/2}]$, assuming T_c is 560 K. (b) The extracted gyromagnetic ratio is plotted as a function of temperature for the YIG/GGG. (c) The calculated Gilbert damping parameter is plotted as a function of temperature. The shaded region represents the 95% confidence interval. (d) The calculated inhomogeneous linewidth is plotted as a function of temperature. The shaded region represents the 95% confidence interval. Note that 1 Oe $= 1 \times 10^3/(4\pi)$ A/m.

and performed a magnetic field sweep at multiple temperatures, such that the data was collected with a finer step size at lower temperature. The temperature-dependent magnetic losses are shown in Fig. 5(a). The temperature-dependent FMR revealed there are additional relaxation channels (not consistent with intrinsic Gilbert-like damping of the YIG) in the LPE grown YIG films evident by the increase in the FMR linewidth at low temperatures in Fig. 5(a). There are several explanations for the increased FMR linewidth at low temperature in the films. One possibility is the influence of a spin-ice state in the GGG substrate due to the hyperkagome lattice configuration of the Gd ions [49]. However, the spin-glass transition temperature is $T_g = 0.14$ K and the spin-liquid state exists at approximately $T = 0.175$ K [50,51], both of which are far below the relevant temperature regimes measured here. Another possibility is the dipolar coupling of the YIG spin waves to the spin system of the paramagnetic GGG substrate [52–54]. This coupling is proportional to $1/T$ [51], while our data show (in Fig. 5) a maximum below 50 K (peaklike dependence) in the FMR linewidth temperature dependence. We therefore conclude that the dominant origin is either fast or slow relaxing impurities [4,55–57]. If there are rare-earth impurities with large orbital momentum in the YIG film, then their exchange coupling with the iron ions introduces an additional relaxation channel into the system. There are fast and slow relaxing impurities; however, most impurities have been experimentally determined to be slow relaxers [4]. For fast-relaxing impurities the characteristic temperature, T_{CH}, is independent of frequency [57,58]. In contrast, for slow relaxing impurities the characteristic temperature, T_{CH}, increases with increasing resonance frequency [57,58]. We distinguish between these two options by examining that T_{CH} might change with frequency. For the 8 GHz frequency the FMR linewidth decreases with decreasing temperature until ∼75 K, then there is a T_{CH} peak in the FMR linewidth at ∼28 K [denoted by the blue line in Fig. 5(a)]. For the 12 GHz frequency the FMR linewidth decreases with decreasing temperature until ∼100 K, then there is a T_{CH} peak in the FMR linewidth at ∼42 K [denoted by the orange line in Fig. 5(a)]. Based on the variation in the T_{CH} between 8 and 12 GHz, we can conclude that there are FMR linewidth contributions present at low temperature due to slowly relaxing impurities in the YIG film; similar results have been reported for YIG spheres [47]. Therefore, we can rule out the fast-relaxing Fe^{2+} and Fe^{4+} ions as contaminants in the YIG films. It is likely the rare-earth impurities come from contaminants from the source materials in the LPE process that may be below the EELS limit of detections (EELS limit of detection claimed here is 0.2 at. % for Gd and other lanthanide series elements). We compared our experimental results for LPE grown YIG films with other results on YIG films reported in literature, namely, Jermain *et al.* [20], Shigematsu *et al.* [59], Fangchiang *et al.* [60], and Liu *et al.* [61]. The comparison is plotted in Fig. 5(b). All these state-of-the-art YIG films display a significant FMR linewidth increase at cryogenic temperatures due to the presence of rare-earth impurities despite their desirable low magnetic damping at room temperature [19,59–61]. Perhaps the most interesting observation is the magnitude of the peaked feature in the linewidth. Specifically, the low-temperature peak in linewidth is negligible for the LPE YIG when compared to other state-of-the-art YIG films in literature, which show approximately an order of magnitude increase in the FMR linewidth at low temperatures. It is likely that one possible source of the impurities in the films of, namely, Jermain *et al.* [20], Shigematsu *et al.* [59], Fangchiang *et al.* [60], and Liu *et al.* [61], is from Gd-ion diffusion from the GGG substrate into the YIG film. The Gd^{3+} is a rare-earth element with ionic radius of 1.05 Å

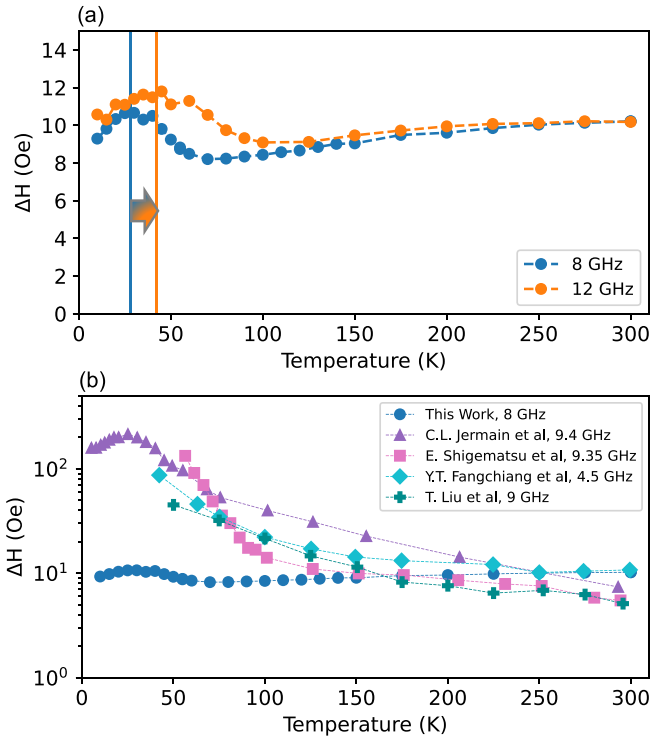

FIG. 5. (a) FMR linewidth at 8 GHz (blue) and 12 GHz (orange) as a function of temperature. The blue line highlights the T_{CH} for 8 GHz rf excitation frequency and the orange highlights the T_{CH} for the 12 GHz excitation frequency. Note that 1 Oe $= 1 \times 10^3/(4\pi)$ A/m. (b) A comparison of the FMR linewidth versus temperature for various YIG/GGG films in literature. The orange arrow is to emphasize the significant difference in magnetic losses. Note that 1 Oe $= 1 \times 10^3/(4\pi)$ A/m.

which is similar to Y^{3+} with ionic radius of 1.02 Å, so that Gd^{3+} may readily replace the Y^{3+} in the YIG lattice. Thus, in the YIG lattice the Gd^{3+} substitutes for the Y^{3+} in the C sites and orders antiparallel to the net moment in the YIG arising from the A and D sites [29]. It is possible that the Gd diffusion is the source of the significant linewidth increase observed at low temperatures for the aforementioned films. The Gd diffusion may be related to the deposition method and temperatures. As previously mentioned, Mitra *et al.* and Cooper *et al.* demonstrated that sputtered YIG suffers from Gd-ion diffusion which influences the bulk magnetic properties at low temperature [29,30]. To confirm this hypothesis further studies are required to investigate the low-temperature FMR linewidth of sputtered and pulsed laser deposited films as a function of thickness and with/without the use of diffusion buffer layers. The suppression of the Gd diffusion in the LPE process may be due to the fundamental differences between this deposition approach and that of pulsed laser deposition and sputtering. LPE growth occurs near equilibrium conditions, while for pulsed laser deposition/sputtering the growth occurs under nonequilibrium conditions and involves atomic species with very high kinetic energy. The equilibrium growth allows for the LPE films to be essentially defect-free, so they have little to no grain boundaries or dislocations. This is consistent with our STEM images (see Supplemental Material Fig. S1) and with previous findings of near microstructural perfection in 11-nm-thin LPE YIG [23,44]; while for the pulsed laser deposited/sputtered films there may be a higher concentration of grain boundaries and dislocations that serve as pathways facilitating impurity diffusion from the GGG substrate into the YIG films, thus promoting greater Gd diffusion depths (interfacial regions on the order of 5-10 nm). Overall, our results revealed that LPE YIG films are minimally affected by slowly relaxing impurities at low temperature likely arising from the suppressed Gd diffusion across the YIG/GGG interface.

III. CONCLUSION

In summary we have studied LPE YIG films (∼48-50 nm thickness) grown on GGG (111) substrates. From the PNR, HAADF-STEM, and STEM-EELS characterizations we determined that there is essentially a sharp interface between the GGG substrate and the LPE YIG film with seemingly significant suppression of Gd diffusion in the YIG film (<1 nm). From the temperature-dependent PNR and FMR we found that the temperature-dependent magnetization in plane is consistent with Bloch's law and does not suggest the emergence of a magnetic dead layer typically seen in cases of Gd-ion diffusion across the YIG/GGG interface [29,30]. The temperature-dependent FMR revealed there are additional relaxation channels (not consistent with intrinsic Gilbert-like damping of the YIG) in the LPE grown YIG films. Since there is a frequency dependence to the impurity characteristic temperature, the relaxation channel was determined to be due to slowly relaxing impurities. The rare-earth impurities in the LPE YIG films are likely due to the Y_2O_3 source material (99.999% purity) as it is near impossible to fully separate rare-earth elements from one another and purify them [33]. While we do observe some contribution to the FMR linewidth at low temperatures due to slowly relaxing impurities, the linewidth increase is insignificant when compared to other state-of-the-art YIG films in literature, which show approximately an order of magnitude higher increase in the FMR linewidth at low temperatures. We attribute the minor impact of slow relaxation in our LPE grown films to the lack of Gd diffusion across the YIG/GGG interface and we believe that sputtered and pulsed laser deposited films suffer from Gd-ion diffusion. Overall, our results revealed that LPE YIG films are impacted minimally by slowly relaxing impurities at low temperature likely arising from the suppressed Gd diffusion across the YIG/GGG interface. Therefore, these films are well suited for cryogenic experiments/applications that require low magnetic losses, such as quantum transduction and manipulation via magnon coupling [38,39,62–64].

ACKNOWLEDGMENTS

A.R.W.-C. and N.X.S. acknowledge financial support from NSF TANMS ERC under Award No. 1160504. A.R.W.-C. was supported by the National Defense Science and Engineering Graduate Fellowship of the Office of Naval Research. This material is based upon work supported by the U.S. Department of Energy, Office of Science, Office of Workforce Development for Teachers and Scientists, Office of Science Graduate Student Research (SCGSR) program. The

SCGSR program is administered by the Oak Ridge Institute for Science and Education (ORISE) for the DOE. ORISE is managed by ORAU under Contract No. DE-SC0014664. All opinions expressed in this paper are the author's and do not necessarily reflect the policies and views of DOE, ORAU, or ORISE. J.L.H. and J.J.C. were funded through the Gordon and Betty Moore Foundation (EPiQS Synthesis Award). This work made use of the Cornell Center for Materials Research Shared Facilities which are supported through the NSF MRSEC program (DMR-1719875). The FEI Titan Themis 300 was acquired through NSF-MRI-1429155, with additional support from Cornell University, the Weill Institute, and the Kavli Institute at Cornell. The work of C.D. was supported by the Deutsche Forschungsgemeinschaft (DFG, German Research Foundation) under Grant No. 271741898. The work of M.L. was supported by the German Bundesministerium für Wirtschaft und Energie (BMWi) under Grant No. 49MF180119. C.D. thanks O. Surzhenko for preliminary studies on FMR characterization of samples at room temperature and R. Meyer (INNOVENT e.V.) for their technical support. A portion of this research used resources at Sandia National Laboratories. Sandia National Laboratories is a multimission laboratory managed and operated by National Technology and Engineering Solutions of Sandia, LLC, a wholly owned subsidiary of Honeywell International Inc., for the U.S. Department of Energy's National Nuclear Security Administration under Contract No. DE-NA0003525. This paper describes objective technical results and analysis. Any subjective views or opinions that might be expressed in the paper do not necessarily represent the views of the U.S. Department of Energy or the United States Government. A portion of this research used resources at the Spallation Neutron Source, a DOE Office of Science User Facility operated by the Oak Ridge National Laboratory. A.R.W.-C. and V.L. thank Haile Ambaye for his assistance during the setup of the PNR experiment. Additionally, any subjective views or opinions that might be expressed in the paper do not necessarily represent the views of NIST.

[1] A. A. Serga, A. V. Chumak, and B. Hillebrands, J. Phys D: Appl. Phys. **43**, 264002 (2010).
[2] A. V. Chumak, V. I. Vasyuchka, A. A. Serga, and B. Hillebrands, Nat. Phys. **11**, 453 (2015).
[3] Y. Kajiwara, K. Harii, S. Takahashi, J. Ohe, K. Uchida, M. Mizuguchi, H. Umezawa, H. Kawai, K. Ando, K. Takanashi, S. Maekawa, and E. Saitoh, Nature (London) **464**, 262 (2010).
[4] M. Sparks, *Ferromagnetic-Relaxation Theory* (McGraw-Hill, New York, 1964).
[5] E. G. Spencer, R. C. LeCraw, and A. M. Clogston, Phys. Rev. Lett. **3**, 32 (1959).
[6] J. Ding, T. Liu, H. Chang, and M. Wu, IEEE Magn. Lett. **11**, 5502305 (2020).
[7] H. Yu, O. d'Allivy Kelly, V. Cros, R. Bernard, P. Bortolotti, A. Anane, F. Brandl, R. Huber, I. Stansinopoulos, and D. Grundler, Sci. Rep. **4**, 6848 (2014).
[8] S. Maendl, I. Stasinopoulos, and D. Grundler, Appl. Phys. Lett. **111**, 012403 (2017).
[9] J. C. Slonczewski, Phys. Rev. B **82**, 054403 (2010).
[10] C. O. Avci, A. Quindeau, C.-F. Pai, M. Mann, L. Caretta, A. S. Tang, M. C. Onbasli, C. A. Ross, and G. S. D. Beach, Nat. Mater. **16**, 309 (2017).
[11] J. M. Bartell, C. L. Jermain, S. V. Aradhya, J. T. Brangham, F. Yang, D. C. Ralph, and G. D. Fuchs, Phys. Rev. Appl. **7**, 044004 (2017).
[12] C. Hahn, G. de Loubens, M. Viret, O. Klein, V. V. Naletov, and J. Ben Youssef, Phys. Rev. Lett. **111**, 217204 (2013).
[13] N. Vlietstra, J. Shan, V. Castel, J. Ben Youssef, G. E. W. Bauer, and B. J. van Wees, Appl. Phys. Lett. **103**, 032401 (2013).
[14] M. Haertinger, C. H. Black, J. Lotze, M. Weiler, S. Geprägs, H. Huebl, S. T. B. Goennenwein, and G. Woltersdorf, Phys. Rev. B. **92**, 054437 (2015).
[15] H. Chang, T. Liu, D. Reifsynder Hickey, P. A. Praveen Janantha, K. Andre Mkhoyan, and M. Wu, APL Mater. **5**, 126104 (2017).
[16] V. Lauer, D. A. Bozhko, T. Brächer, P. Pirro, V. I. Vasyuchka, A. A. Serga, M. B. Jungfleisch, M. Agrawal, Yu. V. Kobljanskyi, G. A. Melkov, C. Dubs, B. Hillebrands, and A. V. Chumak, Appl. Phys. Lett. **108**, 012402 (2016).
[17] Y. Sun, Y.-Y. Song, H. Chang, M. Kabatek, M. Jantz, W. Schneider, M. Wu, H. Schultheiss, and A. Hoffmann, Appl. Phys. Lett. **101**, 152405 (2012).
[18] O. d'Allivy Kelly, A. Anane, R. Bernard, J. Ben Youssef, C. Hahn, A. H. Molpeceres, C. Carretero, E. Jacquet, C. Deranlot, P. Bortolotti, R. Lebourgeois, J.-C. Mage, G. de Loubens, O. Klein, V. Cros, and A. Fert, Appl. Phys. Lett. **103**, 082408 (2013).
[19] M. M. C. Onbasli, A. Kehlberger, D. H. Kim, G. Jakob, M. Klui, A. V. Chumak, B. Hillebrands, and C. A. Ross, APL Mater. **2**, 106102 (2014).
[20] C. L. Jermain, S. V. Aradhya, N. D. Reynolds, R. A. Buhrman, J. T. Brangham, M. R. Page, P. C. Hammel, F. Y. Yang, and D. C. Ralph, Phys. Rev. B **95**, 174411 (2017).
[21] L. V. Lutsev, A. M. Korovin, S. M. Suturin, L. S. Vlasenko, M. P. Volkov, and N. S. Sokolov, J. Phys. D: Appl. Phys. **53**, 265003 (2020).
[22] L. V. Lutsev, A. M. Korovin, V. E. Bursian, S. V. Gastev, V. V. Fedorov, S. M. Suturin, and N. S. Sokolov, Appl. Phys. Lett. **108**, 182402 (2016).
[23] C. Dubs, O. Surzhenko, R. Thomas, J. Osten, T. Schneider, K. Lenz, J. Grenzer, R. Hübner, and E. Wendler, Phys. Rev. Mater. **4**, 024416 (2020).
[24] P. Pirro, T. Brächer, A. V. Chumak, B. Lägel, C. Dubs, O. Surzhenko, P. Görnert, B. Leven, and B. Hillebrands, Appl. Phys. Lett. **104**, 012402 (2014).
[25] A. V. Chumak, P. Kabos, M. Wu, C. Abert, C. Adelmann, A. O. Adeyeye, J. Åkerman, F. G. Alieve, A. Anane, A. Awad *et al.*, IEEE Trans. Magn. **58**, 0800172 (2022).
[26] H. Makino, S. Nakamura, and K. Matsumi, Jpn. J. Appl. Phys. **15**, 415 (1976).
[27] J. R. Carruthers, M. Kokta, R. L. Barns, and M. Grasso, J. Cryst. Growth **19**, 204 (1973).
[28] M. Liu, L. Jin, J. Zhang, Q. Yang, H. Zhang, P. Gao, and D. Yu, AIP Adv. **8**, 085117 (2018).
[29] A. Mitra, O. Cespedes, Q. Ramasse, M. Ali, S. Marmion, M. Ward, R. M. D. Byrdson, C. J. Kinane, J. F. K. Cooper, S. Langridge, and B. J. Hickey, Sci. Rep. **7**, 11774 (2017).

[30] J. F. K. Cooper, C. J. Kinane, S. Langridge, M. Ali, B. J. Hickey, T. Niizeki, K. Uchida, E. Saitoh, H. Ambaye, and A. Glavic, Phys. Rev. B. **96**, 104404 (2017).

[31] A. Talalaevskij, M. Decker, J. Stigloher, A. Mitra, H. S. H. S. Körner, O. Cespedes, C. H. Back, and B. J. Hickey, Phys. Rev. B. **95**, 064409 (2017).

[32] S. M. Suturin, A. M. Korovin, V. E. Bursian, L. V. Lutsev, V. Bourobina, N. L. Yakovlev, M. Montecchi, L. Pasquali, V. Ukleev, A. Vorobiev, A. Devishvili, and N. S. Sokolov, Phys. Rev. Mater. **2**, 104404 (2018).

[33] M. Haidar, M. Ranjbar, M. Balinsky, R. K. Dumas, S. Khartsev, and J. Åkerman, J. Appl. Phys. **117**, 17D119 (2015).

[34] G. F. Dionne and G. L. Fitch, J. Appl. Phys. **87**, 4963 (2000).

[35] J. F. Dillon, Jr. and J. W. Nielsen, Phys. Rev. Lett. **3**, 30 (1959).

[36] L. Lu, Damping mechanisms in magnetic recording materials and microwave-assisted magnetization reversal, PhD thesis, 2016.

[37] L. Jin, Y. Wang, G. Lu, J. Li, Y. He, Z. Zhong, and H. Zhang, AIP Adv. **9**, 025301 (2019).

[38] Y. Li, C. Zhao, W. Zhang, Z. Hoffmann, and V. Novosad, APL Mater. **9**, 060902 (2021).

[39] D. Lachance-Quirion, Y. Tabuchi, A. Gloppe, K. Ussami, and Y. Nakamura, Appl. Phys. Express **12**, 070101 (2019).

[40] C. Dubs, O. Surzhenko, R. Linke, A. Danilewsky, U. Brückner, and J. Dellith, J. Phys. D: Appl. Phys. **50**, 204005 (2017).

[41] Certain commercial equipment, instruments, software, or materials are identified in this paper in order to specify the experimental procedure adequately. Such identifications are not intended to imply recommendation or endorsement by NIST, nor it is intended to imply that the materials or equipment identified are necessarily the best available for the purpose.

[42] V. Lauter-Pasyuk, Soc. Fr. Neutron **7**, s221 (2007).

[43] V. V. Lauter, H. Ambaye, R. Goyette, W. T. Hal Lee, and A. Parizzi, Phys. B (Amsterdam, Neth.) **404**, 2543 (2009).

[44] See Supplemental Material at http://link.aps.org/supplemental/10.1103/PhysRevMaterials.7.054411 for the additional STEM image, and the raw and fitted FMR spectra.

[45] K Lenz, H. Wende, W. Kuch, K. Baberschke, K. Nagy, and A. Jánossy, Phys. Rev. B **73**, 144424 (2006).

[46] A. Okada, S. He, B. Gu, S. Kanai, A. Soumyanarayanan, S. T. Lim, M. Tran, M. Mori, S. Maekawa, F. Matsukura, H. Ohno, and C. Panagopoulos, Proc. Natl Acad. Sci. USA **114**, 3815 (2017).

[47] H. Maier-Flaig, S. Klingler, C. Dubs, O. Surzhenko, R. Gross, M. Weiler, H. Huebl, and S. T. B. Goennenwein, Phys. Rev. B. **95**, 214423 (2017).

[48] S. Mizukami, Y. Ando, and T. Miyazaki, Jpn. J. Appl. Phys. **40**, 580 (2001).

[49] P. P. Deen, O. A. Petrenko, G. Balakrishnan, B. D. Rainford, C. Ritter, L. Capogna, H. Mutka, and T. Fennell, Phys. Rev. B **82**, 174408 (2010).

[50] O. A. Petrenko, G. Balakrishnan, D. McK Paul, M. Yethiraj, and J. Klenke, Appl. Phys. A **74**, S760 (2002).

[51] J. A. M. Paddison, H. Jacobsen, O. A. Petrenko, M. T. Fernández-Díaz, P. P. Deen, and A. L. Goodwin, Science **350**, 179 (2015).

[52] M. G. Balinskii, V. V. Danilov, A. Yu. Nechiporuk, and V. M. Talalaevskii, Radiophys. Quantum Electron **29**, 954 (1986).

[53] V. V. Danilov, A. Yu. Nechiporuk, and L. V. Chevnyuk, Low Temp. Phys. **22**, 802 (1996).

[54] L. Mihalceanu, V. I. Vasyuchka, D. A. Bozhko, T. Langner, A. Y. Nechiporuk, V. F. Romanyuk, B. Hillebrands, and A. A. Serga, Phys. Rev. B **97**, 214405 (2018).

[55] K. P. Belov, L. A. Malevskaya, and V. I. Sokoldv, J. Exp. Theor. Phys. **39**, 1542 (1960) [Sov. Phys. JETP **12**, 1074 (1961)].

[56] A. G. Gurevich and G. A. Melkov, *Magnetization Oscillations and Waves* (CRC Press, Boca Raton, 1996).

[57] S. Kosen, A. F. van Loo, D. A. Bozhko, L. Mihalceanu, and A. D. Karenowska, APL Mater. **7**, 101120 (2019).

[58] A. G. Gurevich and G. A. Melkov, *Magnetization Oscillations and Waves* (CRC Press, Boca Raton, 1996).

[59] E. Shigematsu, Y. Ando, R. Oshima, S. Dushenko, Y. Higuchi, T. Shinjo, H. Jürgen von Bardeleben, and M. Shiraishi, Appl. Phys. Express **9**, 053002 (2016).

[60] Y. T. Fangchiang, K. H. M. Chen, C. C. Tseng, C. C. Chen, C. K. Cheng, S. R. Yang, C. N. Wu, S. F. Lee, M. Hong, and J. Kwo, Nat. Commun. **9**, 223 (2018).

[61] T. Liu, J. Kally, T. Pillsbury, C. Liu, H. Chang, J. Ding, Y. Cheng, M. Hilse, R. Engel-Herbert, A. Richardella, N. Samarth, and M. Wu, Phys. Rev. Lett. **125**, 017204 (2020).

[62] Y. Tabuchi, S. Ishino, A. Noguchi, T. Ishikawa, R. Yamazaki, and Y. Nakamura, Science **349**, 405 (2015).

[63] N. Lauk, N. Sinclair, S. Barzanjeh, J. P. Covey, M. Saffman, M. Spiropulu, and C. Simon, Quantum Sci. Technol. **5**, 020501 (2020).

[64] D. Labanowski, V. Praveen Bhallamudi, Q. Guo, C. M. Purser, B. A. McCaullian, P. Chrus Hammetl, and S. Salahuddin, Sci. Adv. **4**, eaat6574 (2018).